Materials & Design 253 (2025) 113819

Contents lists available at ScienceDirect

Materials & Design

journal homepage: www.elsevier.com/locate/matdes

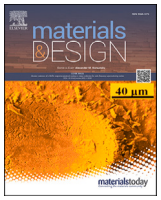

Computational design of mechanical metamaterials through misaligned periodic microstructure

Jiaxin Zhou [a,b], Ikumu Watanabe [a,b,*], Keita Kambayashi [c]

[a] Graduate School of Pure and Applied Sciences, University of Tsukuba, 1-1-1 Tennodai, Tsukuba, Ibaraki 305-8573, Japan
[b] Center for Basic Research on Materials, National Institute for Materials Science, 1-2-1 Sengen, Tsukuba, Ibaraki 305-0047, Japan
[c] Department of Mechanical Engineering, Nagaoka University of Technology, 1603-1 Kamitomioka, Nagaoka, Niigata 940-2188, Japan

ARTICLE INFO

Keywords:
Mechanical metamaterials
Finite element method
Topology optimization
Negative Poisson's ratio
Microstructure design
Misaligned periodicity

ABSTRACT

Mechanical metamaterials, with their intricately designed microstructures, exhibit properties that are superior to those of natural materials. Computational optimization, which uses finite element analysis of periodic microstructures, enables the design of architected microstructures to achieve desired macroscopic properties. Traditionally, unit cells are defined within cuboidal domains; however, this study extends the design to parallelepiped domains, significantly expanding design possibilities. This study investigates the influence of geometric design domains on the topology optimization of negative Poisson's ratio (NPR) metamaterials. Using the mathematical homogenization method, unit cells within parallelogram or parallelepiped domains are represented within square or cubic domains under misaligned periodic boundary conditions. This approach enables the manipulation of macroscopic elastic stiffness components while maintaining the solid volume fraction. A comparative analysis was performed to examine the geometric characteristics of optimized microstructures and the resulting macroscopic anisotropy under both standard and misaligned periodic boundary conditions. 3D-printed NPR metamaterials were tested to validate the design. The results demonstrate the effectiveness of the computational design method in generating diverse microstructures with misalignment, opening new avenues for designing NPR metamaterials with enhanced properties.

1. Introduction

Materials development holds immense potential to revolutionize the creation of innovative devices and systems. While conventional materials possess inherent properties, metamaterials offer unprecedented possibilities by artificially manipulating their internal microstructure to exhibit novel properties not found in nature [1,2]. Recent advancements in high-precision manufacturing techniques, such as 3D printing, have significantly accelerated the realization of metamaterials [3,4]. Moreover, the emergence of computer-oriented design has empowered the creation of intricate metamaterial designs that surpass the limitations of human intuition. These artificially engineered properties span a wide range of domains, including mechanical, acoustic, electromagnetic, and beyond. Furthermore, metamaterials exhibiting synergistically superior multiple properties have been investigated, such as elasto-acoustic metamaterials [5–7]. Driven by the burgeoning field of metamaterials research and development, the mathematical design of mechanical metamaterials has been extensively studied. Notable areas of investigation within this field include metamaterials exhibiting a negative Poisson's ratio (NPR) [8–11], high thermal expansion [12,13], and negative permeability [14,15]. NPR metamaterials, the central focus of this study, possess unique mechanical properties, such as lateral expansion under tension and contraction under compression. These materials exhibit distinct attributes compared to conventional materials, including high resistance to indentation and impact, as well as enhanced energy absorption capabilities. These remarkable properties render them suitable for a variety of applications, encompassing mechanical systems for impact absorption and strain sensing [16–18], electrochemical applications for energy storage [19,20], and biomedical applications [21,22].

To realize mechanical metamaterials, some efforts have relied on design based on human intuition and empirical rules [23–25]; meanwhile, computer-oriented design approaches combining the homogenization method with inverse design techniques have become the mainstream methodology [26]. Mechanical metamaterials, which extend beyond NPR materials, can be achieved by designing the configuration and shape of microscopic structures as internal unit cells and controlling

* Corresponding author at: Graduate School of Pure and Applied Sciences, University of Tsukuba, 1-1-1 Tennodai, Tsukuba, Ibaraki 305-8573, Japan.
E-mail address: WATANABE.Ikumu@nims.go.jp (I. Watanabe).

https://doi.org/10.1016/j.matdes.2025.113819
Received 14 January 2025; Received in revised form 20 February 2025; Accepted 6 March 2025

Available online 20 March 2025

the resulting macroscopic effective mechanical properties through their periodic arrangement. To bridge the gap between the micro- and macro-scales in such multi-scale analysis, the homogenization method is frequently employed, with energy-based and asymptotic methods being common approaches [27–29]. This approach facilitates focus on a Representative Volume Element (RVE) to evaluate macroscopic material properties. In finite element (FE) modeling, a periodic microstructure is considered, and analysis is performed by applying macroscopic stress or strain. This enables the evaluation of material properties under idealized boundary conditions using computational simulations [30,31].

Recently, the application of machine learning to the design of mechanical metamaterials has garnered significant attention, and recent advancements in this regard have been reviewed [2,32–34]. Machine learning-based design approaches enable the exploration of globally optimal solutions and the rapid identification of design solutions that achieve diverse target performances, offering reduced computational costs once trained. However, machine learning for the design of 3D microstructures remains challenging, particularly concerning data preparation and computational demands.

Topology optimization, a sophisticated computer-oriented design method based on the FE method, enables the derivation of material distribution as a solution to a structural optimization problem [35–38]. In contrast with machine learning-based design approaches, this approach is based on the gradient descent method. Therefore, although iterative calculations are required, training data need not be prepared in advance. By combining the FE analysis of an RVE with topology optimization, it is possible to obtain a material microstructure that optimizes macroscopic material properties [39,40]. Furthermore, concurrent optimization of micro- and macro-structures using two-scale FE analysis based on the homogenization method has been reported [41–43]. As a practical issue, design solutions derived from topology optimization have generally been complex and challenging to manufacture. However, in recent years, the feasibility of a one-stop design and manufacturing method based on topology optimization has increased. For instance, the method proposed by Yamada et al. [44] allows for the elimination of closed cavities for stacked fabrication. Despite the computationally prohibitive costs often associated with this approach, recent improvements in computer performance and the development of highly efficient algorithms [45–47] have made industrial applications increasingly feasible.

Topology optimization for NPR metamaterials began with the pioneering work of Sigmund [48]. His seminal study employed homogenization and density-based topology optimization to design an RVE, subsequently arranging these RVEs periodically throughout the spatial domain. Building upon this foundation, Andreassen et al. [49] investigated the design of a manufacturable 3D isotropic elastic NPR metamaterial by employing the solid isotropic material with penalization (SIMP) method along with a robust formulation to ensure a minimum size constraint. Typically, topology optimization for RVE design in NPR metamaterials is confined to cubic design domains. However, periodicity is not inherently limited to cubic arrangements. Zhang et al. [50] examined the influence of the design domain on the 2D design of NPR metamaterials using parallelogram and hexagonal design domains, thus offering diverse possibilities for designing NPR metamaterials. The impact of misalignment can be indirectly inferred by considering a parallelogram domain as a misaligned square domain. Based on the misaligned periodic boundary condition, Li et al. [51] numerically investigated the effect of misalignment on NPR by employing a square unit cell with a star-square feature to demonstrate a direct relationship between NPR and misalignment. Accordingly, the geometry of the periodic design domain influences the outcome of the metamaterial design and can therefore be considered a valuable design variable. Furthermore, by employing non-standard periodic design domains, topology optimization can generate a wider variety of design outcomes. In some cases, this approach can lead to the discovery of microstructures with superior performance or manufacturability. Specifically, incorporating misalignment into the design domain offers a straightforward and effective approach to enhance design diversity.

This study investigated the impact of misalignment within a periodic design domain, explicitly considering it as one of the design variables for the topology optimization-based design of NPR metamaterials. Initially, we investigated this aspect in 2D designs; then, we extended the design methodology to 3D microstructures and experimentally validated the design results using 3D printing. Section 2 introduces the FE analysis method for an RVE to analyze the mechanical behavior of a periodic microstructure, including misaligned periodic boundary conditions in a square or cubic domain. Section 3 presents the topology optimization of a misaligned periodic microstructure for designing NPR metamaterials, where the macroscopic effective Poisson's ratio is formulated for use in the objective function. Section 4 demonstrates the applicability of the proposed method by designing uniaxial, biaxial symmetric, and isotropic metamaterials with targeted NPR values in a 2D design domain. Section 5 extends the design method to a 3D design domain and the resulting designs were fabricated using stereolithography-based 3D printing. Finally, compression tests were performed to validate the material behavior of the designed periodic microstructures.

2. Finite element analysis of representative volume element with misaligned periodic boundary conditions

This section introduces the fundamental boundary value problem for the deformation of a periodic microstructure and its computational solution using the FE method, which facilitates the evaluation of macroscopic mechanical properties from microscopic heterogeneity, considering misaligned periodic boundary conditions.

2.1. Boundary value problem in solid mechanics

For deformation problems of periodic microstructures, the displacement field $\boldsymbol{w}$ is decomposed into a macroscopic homogeneous part $\bar{\boldsymbol{u}}$ and a microscopic periodic part $\boldsymbol{u}$ [29]. The macroscopic homogeneous displacement $\bar{\boldsymbol{u}}$ can be calculated using the macroscopic strain $\bar{\epsilon}$ and the microscale coordinates $\boldsymbol{Y}$ as $\bar{\boldsymbol{u}} = \bar{\epsilon}\boldsymbol{Y}$. The microscopic displacement $\boldsymbol{w}$ and strain $\boldsymbol{\epsilon}$ can be formulated as follows:

$$\boldsymbol{w} = \bar{\boldsymbol{u}} + \boldsymbol{u} = \bar{\epsilon}\boldsymbol{Y} + \boldsymbol{u}, \tag{1}$$

$$\boldsymbol{\epsilon} = \nabla_{\boldsymbol{Y}}\boldsymbol{w} = \bar{\epsilon} + \nabla_{\boldsymbol{Y}}\boldsymbol{u}. \tag{2}$$

The boundary value problem for the microscopic periodic displacement field $\boldsymbol{u}$ is formulated as

$$\int_{\Omega_{\boldsymbol{Y}}} \boldsymbol{\sigma} : \nabla_{\boldsymbol{Y}}\boldsymbol{\eta} d\Omega_{\boldsymbol{Y}} = 0 \quad \forall \boldsymbol{\eta} \in W_{\text{periodic}}, \tag{3}$$

where $\boldsymbol{\sigma}$ is the stress, $\Omega_{\boldsymbol{Y}}$ is the volume of the periodic microstructure, $\boldsymbol{\eta}$ is the variation of periodic displacement $\boldsymbol{u}$, and W_{periodic} is the Sobolev space of periodic functions. Macroscopic variables can be evaluated by volume averaging the corresponding microscopic variables. For example, the macroscopic stress is calculated as

$$\bar{\boldsymbol{\sigma}} := \frac{1}{\Omega_{\boldsymbol{Y}}} \int_{\Omega_{\boldsymbol{Y}}} \boldsymbol{\sigma} d\Omega_{\boldsymbol{Y}}. \tag{4}$$

The boundary value problem (3) is solved using the finite element method. For instance, by applying macroscopic uniaxial stress, the macroscopic stress–strain curve and its microscopic deformation state corresponding to tensile or compression tests can be evaluated. Additionally, by imposing small macroscopic strain modes, the macroscopic stiffness coefficient $\mathbb{C}$ can be evaluated.

2.2. Misaligned periodic boundary condition of RVE

Considering points A and B on opposite sides of a periodic surface, the displacement difference between these points can be expressed as

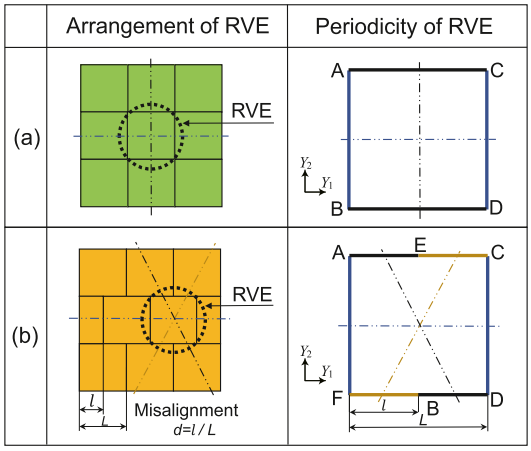

Fig. 1. Illustration of (a) standard and (b) misaligned periodic boundary conditions. Dash-dot lines are used to denote the correspondence within the periodic arrangement.

$$\boldsymbol{w}_{\mathrm{A}} - \boldsymbol{w}_{\mathrm{B}} = \bar{\epsilon}(\boldsymbol{Y}_{\mathrm{A}} - \boldsymbol{Y}_{\mathrm{B}}). \tag{5}$$

Based on Equation (5), the macroscopic homogeneous displacement on the periodic boundary is imposed by controlling the macroscopic strain $\bar{\epsilon}$ as a boundary condition [31]. Equation (5) can be readily applied to the periodicity of an RVE with misalignment. Fig. 1 illustrates standard and misaligned periodic boundary conditions in the horizontal direction, where the misalignment $d \in [0, 0.5]$ is defined as the ratio of the misaligned length l and overall length L of the RVE. The periodic boundary condition considering misalignment in 3D is detailed in Section 5.

3. Topology optimization for designing negative Poisson's ratio metamaterials

In this study, density-based topology optimization was applied to design metamaterial microstructures wherein material distribution within a square or cubic design domain was optimized to achieve an objective function related to macroscopic mechanical properties. This section focuses on presenting the formulation of the Poisson's ratio used in topology optimization. Subsequently, the optimization problem is defined for the topology optimization of NPR metamaterials.

3.1. Formulation of Poisson's ratio

Poisson's ratio is defined as the negative ratio of transverse strain $\epsilon_{\mathrm{trans}}$ to axial strain $\epsilon_{\mathrm{axial}}$ in a uniaxial stress state, that is, $\nu = -\dfrac{\epsilon_{\mathrm{trans}}}{\epsilon_{\mathrm{axial}}}$. In 3D solids, considering a uniaxial stress state along direction a, the strain components $\epsilon_i \; \forall i \in \{1, \cdots 6\}$ can be written as

$$\epsilon_i = D^{-1}_{ia}\sigma_{\mathrm{axial}} \quad \text{for } a \in \{1, 2, 3\}, \tag{6}$$

where $\boldsymbol{D}$ is the stiffness matrix in the vector form of the stress–strain relationship, and σ_{axial} is the uniaxial stress value. In the case of $a = 1$, the Poisson's ratio for the applied stress direction ($a = 1$) is written as

$$\nu_1 = -\frac{\epsilon_2 + \epsilon_3}{2\epsilon_1} = -\frac{D^{-1}_{21} + D^{-1}_{31}}{2D^{-1}_{11}}. \tag{7}$$

Assuming orthotropic elasticity, the above equation can be written using the components of the stiffness matrix D and its fourth order expression $\mathbb{C}$ as

$$\begin{aligned}\nu_1 &= \frac{D_{12}\left(D_{33} - D_{23}\right) + D_{31}\left(D_{22} - D_{23}\right)}{D_{22}D_{33} - D^2_{23}} \\ &= \frac{\mathbb{C}_{1122}\left(\mathbb{C}_{3333} - \mathbb{C}_{2233}\right) + \mathbb{C}_{3311}\left(\mathbb{C}_{2222} - \mathbb{C}_{2233}\right)}{\mathbb{C}_{2222}\mathbb{C}_{3333} - \mathbb{C}^2_{2233}}.\end{aligned} \tag{8}$$

For 2D problems, only in-plane strain was considered, which is equivalent to the plane strain condition. Consequently, the Poisson's ratio of a 2D problem was formulated as

$$\nu_1^{\mathrm{2D}} = \frac{\mathbb{C}_{1122}}{\mathbb{C}_{2222}}. \tag{9}$$

As aforedescribed, the Poisson's ratio of a heterogeneous microstructure for applied stress can be calculated by evaluating the stiffness coefficient $\mathbb{C}$ through FE analysis of the RVE.

3.2. Design problem

Following Equation (8), the design problem for NPR microstructures is formulated as minimizing the difference between the FE analysis-derived macroscopic stiffness coefficient $\bar{\mathbb{C}}_{ijkl}$ and the target values $\mathbb{C}^*_{ijkl}$ by using a weighted-sum multi-objective function [52,53]:

$$\begin{aligned}&\text{Find:} && \rho = \{\rho^e\} \quad \text{for } \rho^e \in [0, 1], \\ &\text{Minimize:} && \mathcal{F} = \sum w_{ijkl}(\bar{\mathbb{C}}_{ijkl} - \mathbb{C}^*_{ijkl})^2, \\ &\text{Subject to:} && \frac{1}{\Omega_{\boldsymbol{Y}}}\int_{\Omega_{\boldsymbol{Y}}} \rho^e d\Omega \le \Omega_{\max},\end{aligned} \tag{10}$$

where ρ^e represents the element density, varying between 0 and 1, and $\Omega_{\max}$ denotes the upper bound of the volume fraction. The term w_{ijkl} represents the weight factor associated with the corresponding stiffness coefficient $\mathbb{C}_{ijkl}$ and is normalized according to the approach outlined in Grodzevich and Romanko [54].

The topology optimization problem was solved using Altair OptiStruct (version 2020, Altair Engineering, Inc., U.S.A.) by employing the SIMP method with a power-law equation for element density penalization. Additionally, mesh dependency was mitigated using a built-in filtering algorithm integrated into the software. The dual method, an efficient and robust algorithm for solving quasi-convex optimization problems, was used to solve the structural optimization problem and determine the optimal design. In the gradient-based topology optimization method, design sensitivity was formulated based on the stiffness component terms in the objective function using the adjoint variable method.

4. Designing negative Poisson's ratio metamaterials in 2D

In this section, the topology optimization design of NPR metamaterials is demonstrated in a 2D square design domain under periodic boundary conditions, considering misalignment, with focus on macroscopic anisotropy.

4.1. Design condition

Topology optimization was performed within a 2D square design domain discretized into a 100 × 100 grid of first-order quadrilateral finite elements. Periodic boundary conditions, as expressed in Equation (5), were applied. Three misalignment cases were considered: $d = 0$, 0.25, and 0.5. Notably, this approach enables the use of the same regular grid mesh for topology optimization across all misalignment cases. In the standard boundary condition case ($d = 0$), a 2 × 2 element region at the center of the design domain was assigned a weaker material property in the initial state. However, in misaligned cases, such artificial irregularity was unnecessary because the resulting design sensitivity tends to be heterogeneous. The properties of the constituent material were as follows: a Young's modulus of 1,000 MPa and a Poisson's ratio of 0.4, which are simple values close to those of an elastic resin after UV curing.

In the topology optimization, the target values of the stiffness coefficient $\mathbb{C}^*_{ijkl}$ were defined, and the following components were set to zero based on the orthotropic assumption:

$$\mathbb{C}_{iiij} = \mathbb{C}_{iiji} = \mathbb{C}_{ijii} = \mathbb{C}_{jiii} \equiv 0 \quad i \neq j \quad (i, j \in \{1, 2\}). \tag{11}$$

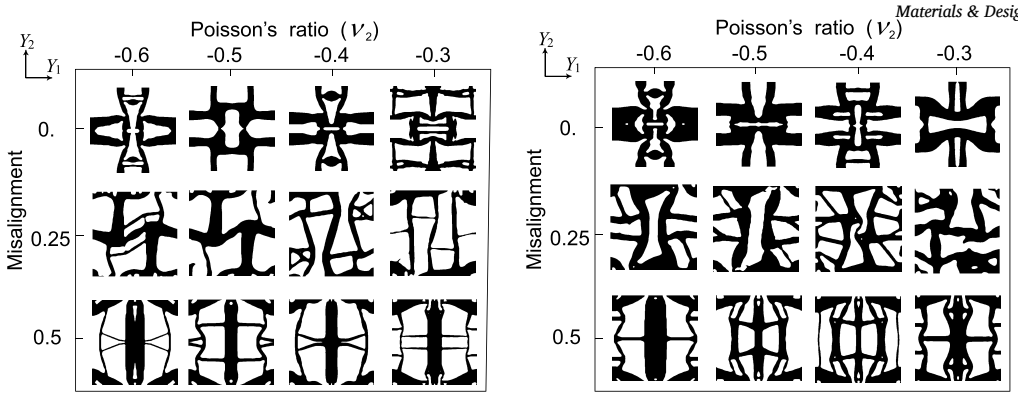

(a) $\Omega_{\max} = 40\%$ (b) $\Omega_{\max} = 50\%$

Fig. 2. Optimal microstructure designs of anisotropic negative Poisson's ratio metamaterials with volume fractions of 40% and 50% under standard and misaligned periodic boundary conditions.

		Optimized microstructure	Microstructure in array	Macroscopic stiffness matrix	NPR mechanism
(a)	d=0	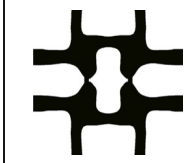		$\begin{bmatrix} 58.16 & -29.27 & 0 \\ -29.27 & 60.90 & 0 \\ 0 & 0 & 4.98 \end{bmatrix}$ ν_2 = -0.503	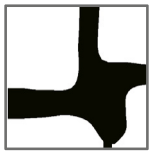
(b)	d=0.25			$\begin{bmatrix} 60.00 & -29.98 & 0 \\ -30.02 & 60.00 & 0 \\ 0 & 0 & 13.01 \end{bmatrix}$ ν_2 = -0.500	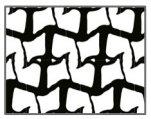
(c)	d=0.5		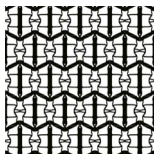	$\begin{bmatrix} 59.84 & -29.74 & 0 \\ -30.22 & 58.53 & 0 \\ 0 & 0 & 1.21 \end{bmatrix}$ ν_2 = -0.505	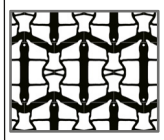

Fig. 3. Comparison of optimal microstructure designs of anisotropic negative Poisson's ratio metamaterials (ν_2 = -0.5) with a volume fraction of 40% under (a) standard and (b, c) misaligned periodic boundary conditions.

4.2. Uniaxial anisotropic design

Anisotropic NPR metamaterials in 2D were designed with varying values of ν_2 under different misalignment conditions. The desired Poisson's ratio was controlled by tuning the macroscopic stiffness coefficient, $\bar{\mathbb{C}}_{1111}$, $\bar{\mathbb{C}}_{1122}$, and $\bar{\mathbb{C}}_{2211}$, following Equation (9). The target values of the macroscopic stiffness coefficient were explored to obtain the optimal structures in all misalignment cases. Fig. 2 presents the optimal designs of periodic microstructures exhibiting $\nu_2 \in [-0.6, -0.3]$ for three different misalignments: $d = 0, 0.25$, and 0.5. These designs were obtained under the upper bounds of 40% and 50% for the volume fraction constraint. The optimized structures generally exhibited volume fractions close to this upper bound. While achieving negative Poisson's ratio characteristics is generally more feasible with lower volume fractions, this can make manufacturing difficult because of decreased stiffness and an increase in the number of thin components. To balance manufacturability with the desired properties, a volume fraction of 40% was adopted for subsequent designs.

Fig. 3 compares the optimal microstructure designs for a target Poisson's ratio of -0.5 and a volume fraction constraint with an upper bound of 40%, under three different misalignment levels: $d = 0, 0.25$, and 0.5. Misalignment introduces non-straight features in the design along the loading direction. In the macroscopic stiffness matrix, $\bar{D}_{22} = \bar{\mathbb{C}}_{2222}$ and $\bar{D}_{44} = \bar{\mathbb{C}}_{1212}$ exhibited different values as they were not explicitly controlled during the topology optimization. Although minor errors (<1%) remain in the macroscopic Poisson's ratio, the calculations converged satisfactorily. The microstructure without misalignment ($d = 0$) revealed a rotating mechanism [8] within the RVE. In contrast, the misaligned microstructure with $d = 0.5$ exhibited a re-entrant mechanism [55] instead. The microstructure with $d = 0.25$ displays intermediate features, showcasing a transition between these two mechanisms. The deformation mechanism can be altered without changing the volume fraction or target Poisson's ratio, simply by adjusting the misalignment. However, it is important to note that the deformation mechanism is not solely determined by the misalignment. For instance, Zhang and Khandelwal (2019) [50] demonstrated the design of NPR structures with diverse deformation mechanisms by varying design conditions across different geometries of design domain.

Next, deformation analyses were conducted by applying uniaxial stress $\bar{\sigma}_2$ to investigate the mechanical behavior of the designed NPR metamaterial microstructures under large deformation. Fig. 4 illustrates the deformation state with distributions of equivalent strain, defined as $\epsilon^* = \sqrt{2/3}\|\mathrm{dev}[\boldsymbol{\epsilon}]\|$. As shown in Fig. 4, negative transverse deformation was observed in all three cases. In the case of $d = 0.5$, a pronounced

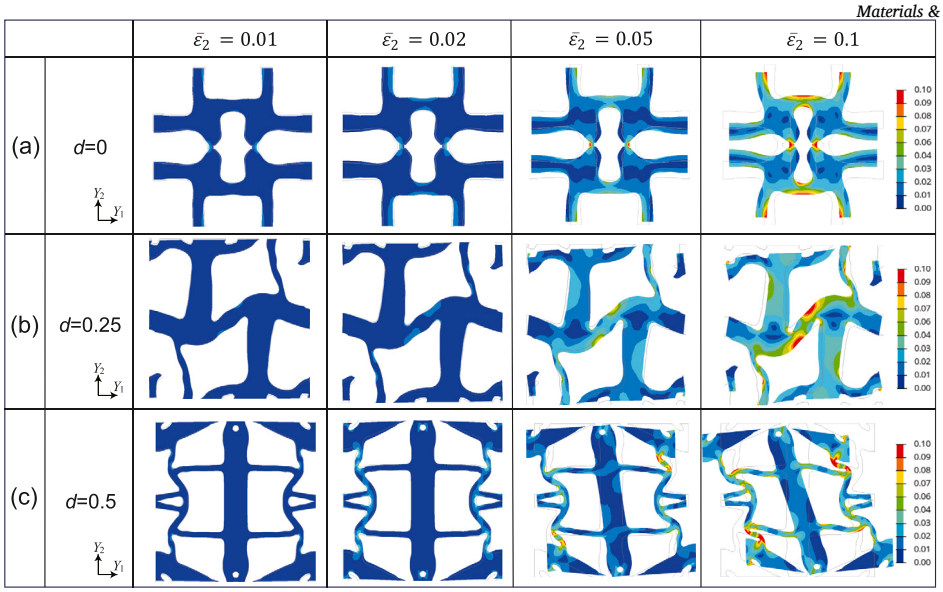

Fig. 4. Deformation states and equivalent strain distributions of anisotropic microstructure designs of negative Poisson's ratio metamaterials under (a) standard and (b, c) misaligned periodic boundary conditions.

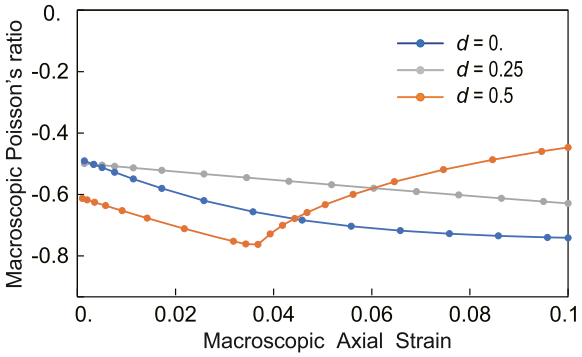

Fig. 5. Relationships between macroscopic Poisson's ratio and axial strain of anisotropic microstructure designs of negative Poisson's ratio metamaterials under standard and misaligned periodic boundary conditions.

shear deformation mode appeared despite the decoupling of axial and shear effects in Equation (11). This is attributed to the low macroscopic shear stiffness, represented by $\bar{\mathbb{C}}_{1212}$. Fig. 5 presents the relationships between the macroscopic Poisson's ratio, calculated using Equation (9), and axial strain. The values of Poisson's ratio initially coincided with the designed values and then gradually decreased with increasing macroscopic axial strain in the cases of $d = 0$ and 0.25. In contrast, for $d = 0.5$, the Poisson's ratio initially deviated from the designed value and subsequently exhibited a sudden increase during the deformation. The nonlinear behavior is attributable to the shear deformation mode. Notably, the design is based on small strain theory; therefore, the actual behavior at finite strain may deviate from the design predictions. The observed nonlinear behavior in the case of $d = 0.5$ was likely induced by the misalignment.

4.3. Biaxial symmetric design

In the preceding uniaxial anisotropic designs, the macroscopic stiffness coefficient $\bar{\mathbb{C}}_{1111}$, $\bar{\mathbb{C}}_{1122}$, and $\bar{\mathbb{C}}_{2211}$ were considered in the objective function. For the subsequent biaxial symmetric designs, the component $\bar{\mathbb{C}}_{2222}$ was additionally incorporated. The target Poisson's ratio was set to -0.4 under a volume fraction constraint of 40%, with the target macroscopic stiffness matrix defined as follows:

$$\boldsymbol{D}^* = \begin{bmatrix} 100 & -40 & 0 \\ & 100 & 0 \\ \text{sym.} & & * \end{bmatrix} \quad \text{for} \quad \nu_1 = \nu_2 = -0.4, \tag{12}$$

where $*$ represents an arbitrary value.

Fig. 6 presents the optimal designs arranged in a 5 × 5 array, accompanied by the corresponding macroscopic stiffness matrices. The periodic microstructures exhibited distinct mechanisms: a rotating mechanism under standard periodic boundary conditions and a re-entrant mechanism under misaligned periodic boundary conditions, similar to those observed in the uniaxial anisotropic designs. Additionally, Fig. 6 depicts a summary of the resulting Poisson's ratio and Zener anisotropic ratio. The Zener anisotropic ratio, as defined in 2D, is expressed as:

$$a_r = \frac{4\mathbb{C}_{1212}}{\mathbb{C}_{1111} + \mathbb{C}_{2222} - \mathbb{C}_{1122} - \mathbb{C}_{2211}}. \tag{13}$$

Based on the Zener ratio, these microstructures exhibit strong anisotropy.

4.4. Isotropic design

Lastly, periodic microstructures of isotropic NPR metamaterials were designed by controlling the macroscopic stiffness coefficients $\bar{\mathbb{C}}_{iiii}$, $\bar{\mathbb{C}}_{iijj}$, and $\bar{\mathbb{C}}_{ijij}$ $(i, j = \{1, 2\})$ in topology optimization. The target Poisson's ratio was set to -0.4 under a volume fraction constraint of 40%, with the target macroscopic stiffness matrix defined as follows:

$$\boldsymbol{D}^* = \begin{bmatrix} 50 & -15 & 0 \\ & 50 & 0 \\ \text{sym.} & & 32.5 \end{bmatrix} \quad \text{for} \quad \nu_1 = \nu_2 = -0.4 \quad \text{and} \quad a_r = 1 \tag{14}$$

Fig. 7 presents the optimal designs with a 5 × 5 array arrangement, along with the resulting macroscopic stiffness matrices and the corresponding properties. Notably, microstructures with isotropic properties were successfully obtained, even in the misaligned cases. Achieving the target properties with high accuracy in these cases can be challenging, primarily owing to the need to control multiple components of the macroscopic stiffness coefficients within the objective function (Equation (10)).

The results demonstrate that misalignment in the periodic boundary condition allows for the design of microstructures with identical macroscopic properties but distinct morphologies and deformation mechanisms. This highlights misalignment as a valuable design variable that can introduce diversity into metamaterial design.

		Optimized microstructure	Microstructure in array	Macroscopic stiffness matrix	Properties
(a)	d=0		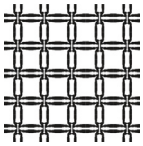	$\begin{bmatrix} 99.93 & -39.90 & 0 \\ -39.90 & 99.76 & 0 \\ 0 & 0 & 2.61 \end{bmatrix}$	ν_1 = -0.40 ν_2 = -0.40 a_r = 0.037
(b)	d=0.25		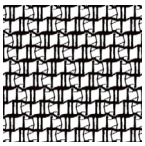	$\begin{bmatrix} 99.91 & -39.54 & 0 \\ -40.26 & 99.90 & 0 \\ 0 & 0 & 0.351 \end{bmatrix}$	ν_1 = -0.40 ν_2 = -0.40 a_r = 0.005
(c)	d=0.5			$\begin{bmatrix} 99.91 & -38.61 & 0 \\ -41.37 & 100.15 & 0 \\ 0 & 0 & 1.38 \end{bmatrix}$	ν_1 = -0.39 ν_2 = -0.41 a_r = 0.020

Fig. 6. Optimal microstructure designs of biaxial symmetric negative Poisson's ratio metamaterials with a volume fraction of 40% under (a) standard and (b, c) misaligned periodic boundary conditions.

		Optimized microstructure	Microstructure in array	Macroscopic stiffness matrix	Properties
(a)	d=0		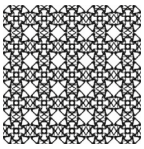	$\begin{bmatrix} 49.93 & -14.90 & 0 \\ -14.90 & 49.93 & 0 \\ 0 & 0 & 32.42 \end{bmatrix}$	ν_1 = -0.30 ν_2 = -0.30 a_r =1.000
(b)	d=0.25			$\begin{bmatrix} 49.94 & -14.77 & 0 \\ -15.10 & 49.98 & 0 \\ 0 & 0 & 32.50 \end{bmatrix}$	ν_1 = -0.30 ν_2 = -0.30 a_r =1.002
(c)	d=0.5		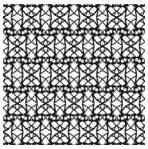	$\begin{bmatrix} 49.65 & -14.48 & 0 \\ -15.23 & 49.73 & 0 \\ 0 & 0 & 32.41 \end{bmatrix}$	ν_1 = -0.29 ν_2 = -0.31 a_r =1.004

Fig. 7. Optimal microstructure designs of isotropic negative Poisson's ratio metamaterials with a volume fraction of 40% under (a) standard and (b, c) misaligned periodic boundary conditions.

5. 3D design of negative Poisson's ratio metamaterials

Based on the results from Section 4, 3D NPR periodic microstructures were designed considering misalignment in the periodic design domain during topology optimization. The designed metamaterials were then validated through experimental compression tests using 3D-printed samples.

5.1. Design conditions

The design domain was discretized into a 64 × 64 × 64 grid of first-order hexahedral finite elements. Periodic boundary conditions, as derived in Equation (5), were applied. Fig. 8 shows the setting of periodic boundary conditions. In the misaligned case, a complex periodicity was considered on the top and bottom surfaces. Two misalignments, d_1 and d_2, were defined, as shown in Fig. 8(b), where the line and area pairs of periodicity are summarized. Notably, instead of the simple pairing observed in the standard periodicity shown in Fig. 8(a), four area pairs were aligned diagonally across the top and bottom surfaces. This study focuses on rectangular cuboid domains. However, other types of misalignments can be explored in different space-filling periodic structures. Furthermore, non-design regions were defined within the design domain, as shown in Fig. 9. The periodic pattern facilitates the generation of higher-order microstructures, enabling internal deformation modes such as rotating and re-entrant deformation mechanisms.

In this study, 3D microstructures with cubic symmetry and a Poisson's ratio of -0.4 were designed for both standard and misaligned periodic boundary conditions. The misalignment was set to 0.5 in both the Y_1 and Y_2 directions (i.e., $d_1 = d_2 = 0.5$). The properties of the constituent material were identical to those used in the 2D design. The target stiffness matrix with a volume fraction of 40% was set as follows:

$$\boldsymbol{D}^* = \begin{bmatrix} 0.49 & -0.14 & -0.14 & * & * & * \\ & 0.49 & -0.14 & * & * & * \\ & & 0.49 & * & * & * \\ & \text{sym.} & & * & * & * \\ & & & & * & * \\ & & & & & * \end{bmatrix}. \tag{15}$$

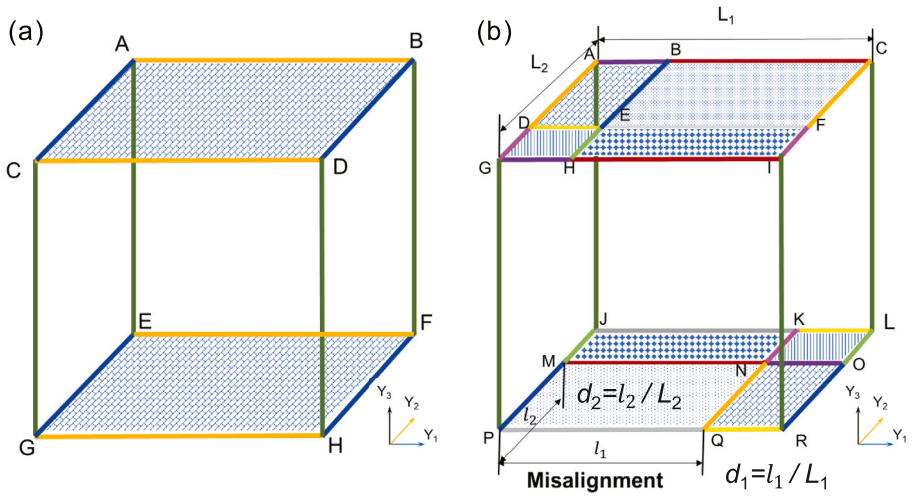

Fig. 8. Configurations of (a) standard and (b) misaligned periodic boundary conditions in a 3D design domain.

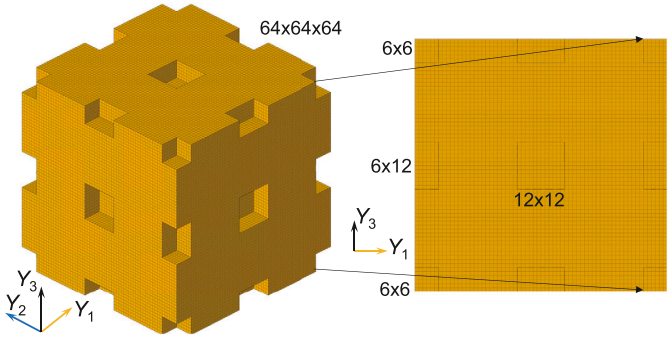

Fig. 9. Non-design regions in the 3D design domain.

This limited set of target values was chosen to ensure accurate results in the topology optimization.

5.2. Design results

Fig. 10 presents the design results of the NPR microstructures derived through topology optimization. It showcases both individual unit cells and 3×3×3 array microstructures. The major values of the resulting macroscopic stiffness matrices, as well as the corresponding NPR values for different applied stress directions and Zener anisotropic ratios, are presented in Fig. 10. In the 3D topology optimization, achieving accurate convergence to the target values posed a challenging. While computational residuals increased in the 3D design process, the results remained closely aligned with the target values, with deviations of less than 10%.

To further illustrate the directional dependency, Fig. 11 presents polar plots of Poisson's ratio, which were calculated using the macroscopic stiffness matrices. In these plots, red and blue colors represent positive and negative values, respectively. Cubic symmetry is evident in both microstructures, with negative Poisson's ratios observed only along the three axial directions. For all other loading directions, the material response is not auxetic. As discussed in Section 4, controlling the shear components of the macroscopic stiffness coefficient is crucial for obtaining isotropic microstructures.

Subsequently, deformation analyses were performed by applying uniaxial stress along each orthogonal axis (Y_1, Y_2, and Y_3) to investigate the mechanical behavior of the designed NPR metamaterial microstructures under large deformations. Fig. 12 depicts the finite element meshes of the designed microstructure, wherein one-eighth of the volume has been rendered transparent to visualize the interior structure, along with the deformation state and equivalent strain distributions. Fig. 13 illustrates the relationships between the macroscopic Poisson's ratio, calculated using Equation (8), and axial strain. Consistent with the 2D results presented in Fig. 5, the values of Poisson's ratio initially aligned with the designed value but subsequently diverged with increasing macroscopic axial strain in the both cases owing to the effect of finite strain.

5.3. Experimental validation

The 3×3×3 array microstructures of designed unit cells were fabricated using an elastic photopolymer resin (Elastic 50A resin, Formlabs, USA) and a 3D printer (Form 3, Formlabs, USA). The specimens had dimensions of 4 cm × 4 cm × 4 cm. After a 15-min wash with isopropanol, the 3D–printed specimens were fully cured at 60 °C for 20 mins. The mechanical properties of the fabricated specimens were subsequently evaluated through static compression tests, which were conducted in three orthogonal directions using a motorized test stand (AGXplus-10 kN, Shimadzu, Japan). While compression tests were primarily used in this study, the designed microstructures, derived through topology optimization, also exhibit NPR behavior when subjected to tensile tests [53]. The specimens were subjected to uniaxial compression at a constant displacement rate of 10 mm/min during both loading and unloading, reaching a maximum axial strain of 0.2. Sequential images of the deforming samples were captured during the experiments to evaluate the deformation state and calculate Poisson's ratio in post-processing.

Fig. 14 illustrates the fabricated microstructures and their deformation behaviors. Notably, negative transverse deformation was observed across all cases. The deformation patterns evident in each unit cell demonstrate agreement with those predicted via numerical simulations, as presented in Fig. 12. In the case of compression along the Y_2 direction for the misaligned microstructure, structural buckling became apparent due to the boundary condition imposed at the sample surface during the compression test. While this effect could potentially be mitigated through the use of larger arrays, it is noteworthy that NPR behavior was still consistently observed, even in the presence of this issue. Fig. 15 presents the axial stress–strain curves for the 3D-printed NPR metamaterial samples, as derived from the compression tests. For the sample designed under the standard periodic boundary condition, the stress–strain curves exhibited near identity across all loading directions up to an axial strain of 0.1. In contrast, for the sample designed under the misaligned periodic boundary condition, the responses were distinctly categorized into two groups: parallel (Y_1 and Y_2) and perpendicular (Y_3) directions to the surface defining the misaligned boundary condition. This behavior is attributed primarily not to the aforementioned

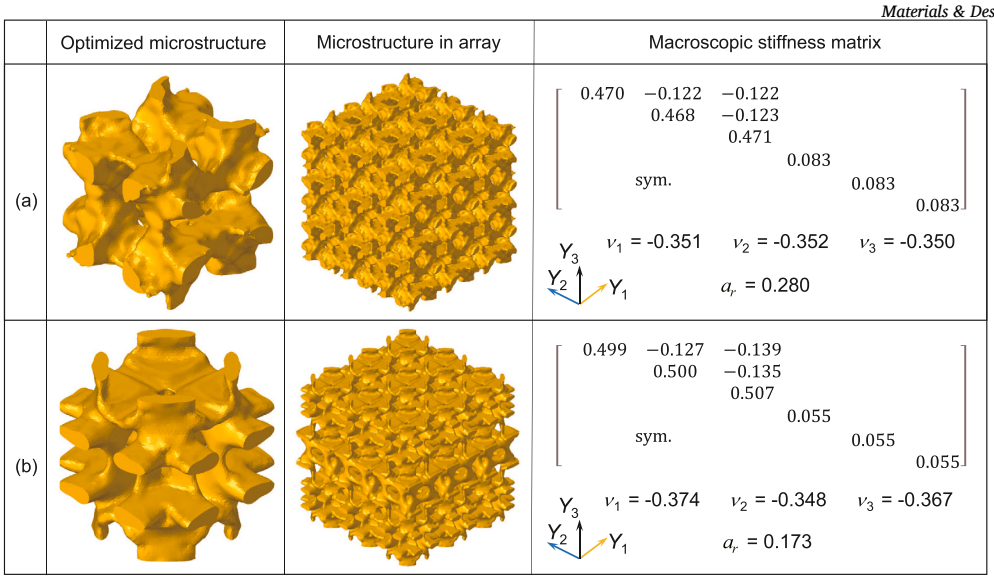

Fig. 10. Optimal microstructure designs of 3D negative Poisson's ratio metamaterials with a volume fraction of 40% under (a) standard and (b) misaligned periodic boundary conditions.

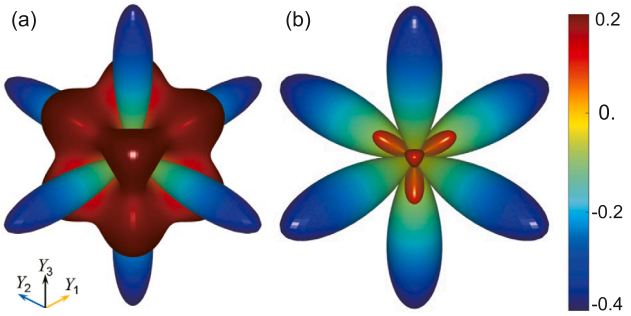

Fig. 11. Polar plots of Poisson's ratio in optimized microstructures under (a) standard and (b) misaligned periodic boundary conditions.

Table 1
Experimental results: Poisson's ratio at axial strain 20 %.

Misalignment	Compression direction	Transverse strain	2D Poisson's ratio
$d_1 = d_2 = 0$	Y_1	0.081	-0.405
	Y_2	0.072	- 0.36
	Y_3	0.084	-0.42
$d_1 = d_2 = 0.5$	Y_1	0.043	-0.215
	Y_2	0.060	- 0.30
	Y_3	0.069	-0.345

structural buckling, but rather to the inherent microstructure geometry arising from the misalignment. Table 1 summarizes the measured transverse strain and Poisson's ratio. The Poisson's ratio was calculated from the transverse and axial strains, consistent with the definition of the two-dimensional Poisson's ratio in Equation (9). In the case of $d_1 = d_2 = 0$, the target Poisson's ratio was achieved. Despite the aforedescribed unexpected material behaviors observed in the misaligned case, the sample still exhibited NPR characteristics.

6. Conclusion

This study integrated finite element analysis method of a periodic microstructure with topology optimization for designing NPR metamaterials. Notably, based on the expansion capability of the periodic boundary condition, the effect of misalignment in the design domain was investigated to enhance design potential. The misalignment resulted in non-straight material distributions in the optimal designs; consequently, the deformation mechanism of NPR changed, even with the same material properties. Therefore, misalignment emerges as a significant design variable in topology optimization. This design concept is broadly applicable beyond NPR metamaterials, extending to the design of other mechanical metamaterials. This study contributes to advancing the research and development of smart metamaterials.

CRediT authorship contribution statement

Jiaxin Zhou: Writing – review & editing, Writing – original draft, Visualization, Validation, Methodology, Investigation, Funding acquisition, Formal analysis, Data curation, Conceptualization. **Ikumu Watanabe:** Writing – review & editing, Visualization, Supervision, Software, Resources, Project administration, Methodology, Investigation, Conceptualization. **Keita Kambayashi:** Writing – review & editing, Methodology, Investigation.

Declaration of competing interest

The authors declare that they have no known competing financial interests or personal relationships that could have appeared to influence the work reported in this paper.

Acknowledgement

This study was supported by the Japan Science and Technology Agency – Supporting Program for Innovative Research on Cutting-Edge Science and Technology (SPRING), Grant Number JPMJSP2124, and the Altair Research Support program. The authors wish to acknowledge Ms. Y. Yamamoto of the National Institute for Materials Science for her technical support. We would like to thank Editage for English language editing.

Data availability

Data will be made available on request.

References

[1] J.E. Holliman, H.T. Schaef, B.P. McGrail, Q.R.S. Miller, Review of foundational concepts and emerging directions in metamaterial research: design, phenomena, and applications, Mater. Adv. 3 (2022) 8390–8406, https://doi.org/10.1039/D2MA00497F.

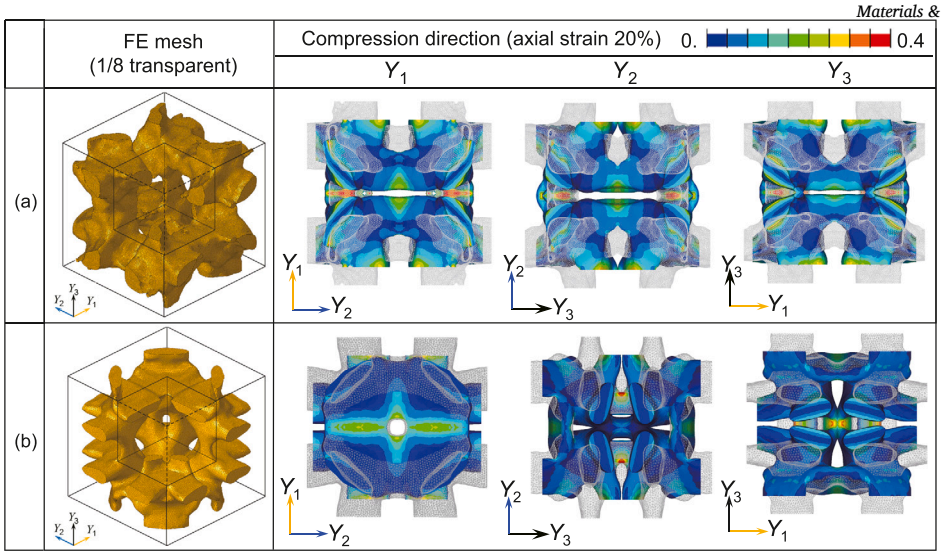

Fig. 12. Deformation states and equivalent strain distributions of 3D microstructure designs of negative Poisson's ratio metamaterials under (a) standard and (b) misaligned periodic boundary conditions. In FE meshes, one-eighth of the volume is rendered transparent to reveal the interior structure.

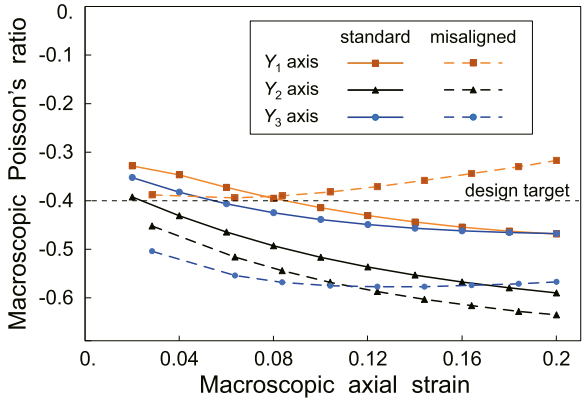

Fig. 13. Relationships between macroscopic Poisson's ratio and axial strain of 3D microstructure designs of negative Poisson's ratio metamaterials under standard and misaligned periodic boundary conditions.

[2] P. Jiao, J. Mueller, J.R. Raney, X. Zheng, A.H. Alavi, Mechanical metamaterials and beyond, Nat. Commun. 14 (1) (2023) 6004, https://doi.org/10.1038/s41467-023-41679-8.

[3] M. Askari, D.A. Hutchins, P.J. Thomas, L. Astolfi, R.L. Watson, M. Abdi, M. Ricci, S. Laureti, L. Nie, S. Freear, R. Wildman, C. Tuck, M. Clarke, E. Woods, A.T. Clare, Additive manufacturing of metamaterials: a review, Addit. Manuf. 36 (2020) 101562, https://doi.org/10.1016/j.addma.2020.101562.

[4] J. Fan, L. Zhang, S. Wei, Z. Zhang, S.-K. Choi, B. Song, Y. Shi, A review of additive manufacturing of metamaterials and developing trends, Mater. Today 50 (2021) 303–328, https://doi.org/10.1016/j.mattod.2021.04.019.

[5] P. Sun, H. Guo, F. Jin, Z. Zhang, N. Liu, T. Yuan, L. Ma, Y. Wang, Mechanics and extreme low-frequency band gaps of auxetic hexachiral acoustic metamaterial with internal resonant unit, Appl. Acoust. 200 (2022) 109046, https://doi.org/10.1016/j.apacoust.2022.109046.

[6] M. Wang, A. Pau, M. Lepidi, Elastoacoustic wave propagation in a biphasic mechanical metamaterial, J. Acoust. Soc. Am. 155 (5) (2024) 3322–3335, https://doi.org/10.1121/10.0026079.

[7] Z. Hu, J. Ding, S. Ding, W.W.S. Ma, J.W. Chua, X. Li, W. Zhai, X. Song, Machine learning–enabled inverse design of shell-based lattice metamaterials with optimal sound and energy absorption, Virtual Phys. Prototyping 19 (1) (2024) e2412198, https://doi.org/10.1080/17452759.2024.2412198.

[8] J. Gao, H. Xue, L. Gao, Z. Luo, Topology optimization for auxetic metamaterials based on isogeometric analysis, Comput. Methods Appl. Mech. Eng. 352 (2019) 211–236, https://doi.org/10.1016/j.cma.2019.04.021.

[9] F. Wang, O. Sigmund, J.S. Jensen, Design of materials with prescribed nonlinear properties, J. Mech. Phys. Solids 69 (2014) 156–174, https://doi.org/10.1016/j.jmps.2014.05.003.

[10] F. Wang, Systematic design of 3d auxetic lattice materials with programmable Poisson's ratio for finite strains, J. Mech. Phys. Solids 114 (2018) 303–318, https://doi.org/10.1016/j.jmps.2018.01.013.

[11] Z. Li, W. Gao, M.Y. Wang, C.H. Wang, Z. Luo, Three-dimensional metamaterials exhibiting extreme isotropy and negative Poisson's ratio, Int. J. Mech. Sci. 259 (2023) 108617, https://doi.org/10.1016/j.ijmecsci.2023.108617.

[12] O. Sigmund, S. Torquato, Design of materials with extreme thermal expansion using a three-phase topology optimization method, J. Mech. Phys. Solids 45 (6) (1997) 1037–1067, https://doi.org/10.1016/S0022-5096(96)00114-7.

[13] W. Sha, M. Xiao, Y. Wang, M. Huang, Q. Li, L. Gao, Topology optimization methods for thermal metamaterials: a review, Int. J. Heat Mass Transf. 227 (2024) 125588, https://doi.org/10.1016/j.ijheatmasstransfer.2024.125588.

[14] A.R. Diaz, O. Sigmund, A topology optimization method for design of negative permeability metamaterials, Struct. Multidiscip. Optim. 41 (2010) 163–177, https://doi.org/10.1007/s00158-009-0416-y.

[15] S. Zhou, W. Li, Y. Chen, G. Sun, Q. Li, Topology optimization for negative permeability metamaterials using level-set algorithm, Acta Mater. 59 (7) (2011) 2624–2636, https://doi.org/10.1016/j.actamat.2010.12.049.

[16] S. Yuan, F. Shen, J. Bai, C.K. Chua, J. Wei, K. Zhou, 3D soft auxetic lattice structures fabricated by selective laser sintering: TPU powder evaluation and process optimization, Mater. Des. 120 (2017) 317–327, https://doi.org/10.1016/j.matdes.2017.01.098.

[17] D.H. Le, Y. Xu, M.M. Tentzeris, S. Lim, Transformation from 2d meta-pixel to 3d meta-pixel using auxetic Kirigami for programmable multifunctional electromagnetic response, Extrem. Mech. Lett. 36 (2020) 100670, https://doi.org/10.1016/j.eml.2020.100670.

[18] Y. Jiang, Z. Liu, N. Matsuhisa, D. Qi, W.R. Leow, H. Yang, X. Chen, Auxetic mechanical metamaterials to enhance sensitivity of stretchable strain sensors, Adv. Mater. 30 (12) (2018) 1706589, https://doi.org/10.1002/adma.201706589.

[19] L. Weng, J. Zhou, R. Cai, Analytical model of li-ion diffusion-induced stress in nanowire and negative Poisson's ratio electrode under different operations, Int. J. Mech. Sci. 141 (2018) 245–261, https://doi.org/10.1016/j.ijmecsci.2018.04.013.

[20] P. Chang, H. Mei, Y. Tan, Y. Zhao, W. Huang, L. Cheng, A 3d-printed stretchable structural supercapacitor with active stretchability/flexibility and remarkable volumetric capacitance, J. Mater. Chem. A 8 (27) (2020) 13646–13658, https://doi.org/10.1039/D0TA04460A.

[21] H.M. Kolken, S. Janbaz, S.M. Leeflang, K. Lietaert, H.H. Weinans, A.A. Zadpoor, Rationally designed meta-implants: a combination of auxetic and conventional meta-biomaterials, Mater. Horiz. 5 (1) (2018) 28–35, https://doi.org/10.1039/C7MH00699C.

[22] A.A. Zadpoor, Mechanical performance of additively manufactured meta-biomaterials, Acta Biomater. 85 (2019) 41–59, https://doi.org/10.1016/j.actbio.2018.12.038.

[23] A. Sorrentino, D. Castagnetti, L. Mizzi, A. Spaggiari, Bio-inspired auxetic mechanical metamaterials evolved from rotating squares unit, Mech. Mater. 173 (2022) 104421, https://doi.org/10.1016/j.mechmat.2022.104421.

[24] A. Sorrentino, D. Castagnetti, Novel polyhedral mechanical metamaterial exhibiting negative Poisson's ratio, Smart Mater. Struct. 32 (3) (2023) 035008, https://doi.org/10.1088/1361-665X/acb3a3.

[25] A. Sorrentino, D. Castagnetti, Periodic tetrahedral auxetic metamaterial, Extrem. Mech. Lett. 71 (2024) 102214, https://doi.org/10.1016/j.eml.2024.102214.

[26] J. Gao, X. Cao, M. Xiao, Z. Yang, X. Zhou, Y. Li, L. Gao, W. Yan, T. Rabczuk, Y. Mai, Rational designs of mechanical metamaterials: formulations, architectures,

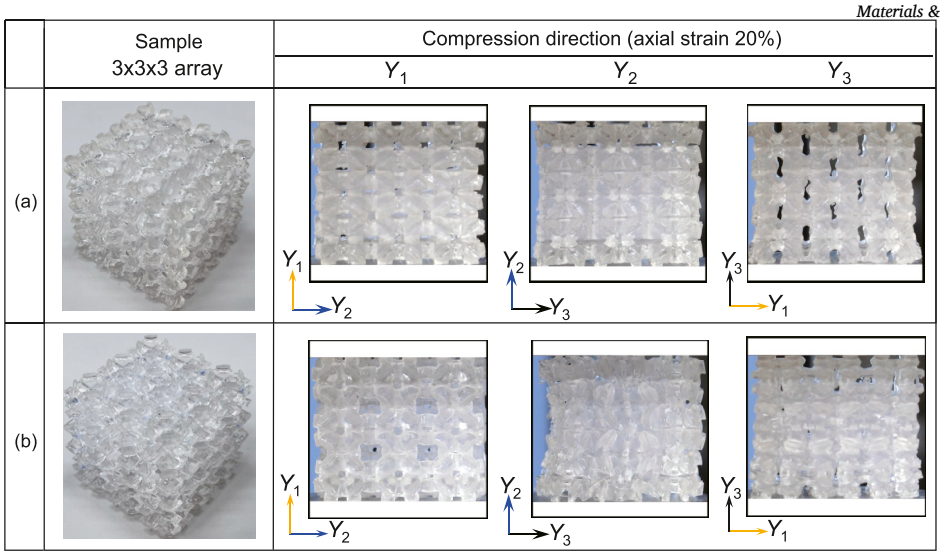

Fig. 14. Deformation states of 3D-printed NPR metamaterial samples in compression tests at axial strain 20%.

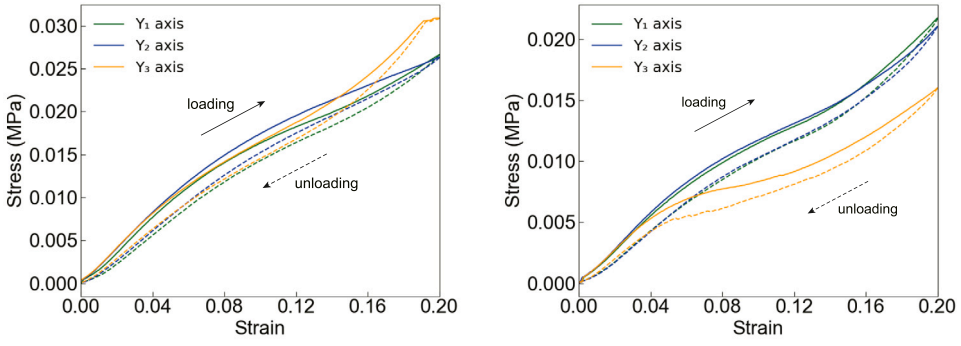

(a) $d_1 = d_2 = 0$ (b) $d_1 = d_2 = 0.5$

Fig. 15. Axial stress–strain curves of 3D-printed NPR metamaterial samples in compression tests. Solid and dotted lines show loading and unloading curves, respectively.

tessellations and prospects, Mater. Sci. Eng., R Rep. 156 (2023) 100755, https://doi.org/10.1016/j.mser.2023.100755.

[27] C. Miehe, J. Schröder, J. Schotte, Computational homogenization analysis in finite plasticity simulation of texture development in polycrystalline materials, Comput. Methods Appl. Mech. Eng. 171 (3) (1999) 387–418, https://doi.org/10.1016/S0045-7825(98)00218-7.

[28] K. Terada, N. Kikuchi, A class of general algorithms for multi-scale analyses of heterogeneous media, Comput. Methods Appl. Mech. Eng. 190 (40) (2001) 5427–5464, https://doi.org/10.1016/S0045-7825(01)00179-7.

[29] K. Terada, I. Saiki, K. Matsui, Y. Yamakawa, Two-scale kinematics and linearization for simultaneous two-scale analysis of periodic heterogeneous solids at finite strain, Comput. Methods Appl. Mech. Eng. 192 (31) (2003) 3531–3563, https://doi.org/10.1016/S0045-7825(03)00365-7.

[30] I. Watanabe, D. Setoyama, N. Nagasako, N. Iwata, K. Nakanishi, Multiscale prediction of mechanical behavior of ferrite–pearlite steel with numerical material testing, Int. J. Numer. Methods Eng. 89 (7) (2012) 829–845, https://doi.org/10.1002/nme.3264.

[31] I. Watanabe, A. Yamanaka, Voxel coarsening approach on image-based finite element modeling of representative volume element, Int. J. Mech. Sci. 150 (2019) 314–321, https://doi.org/10.1016/j.ijmecsci.2018.10.028.

[32] K. Guo, Z. Yang, C.-H. Yu, M.J. Buehler, Artificial intelligence and machine learning in design of mechanical materials, Mater. Horiz. 8 (4) (2021) 1153–1172, https://doi.org/10.1039/D0MH01451F.

[33] X. Zheng, X. Zhang, T. Chen, I. Watanabe, Deep learning in mechanical metamaterials: from prediction and generation to inverse design, Adv. Mater. 35 (45) (2023) 2302530, https://doi.org/10.1002/adma.202302530.

[34] D. Lee, W.W. Chen, L. Wang, Y.-C. Chan, W. Chen, Data-driven design for metamaterials and multiscale systems: a review, Adv. Mater. 36 (8) (2024) 2305254, https://doi.org/10.1002/adma.202305254, https://onlinelibrary.wiley.com/doi/pdf/10.1002/adma.202305254.

[35] M.P. Bendsøe, Optimal shape design as a material distribution problem, Struct. Optim. 1 (1989) 193–202, https://doi.org/10.1007/BF01650949.

[36] M. Zhou, G.I. Rozvany, The coc algorithm, part ii: topological, geometrical and generalized shape optimization, Comput. Methods Appl. Mech. Eng. 89 (1–3) (1991) 309–336, https://doi.org/10.1016/0045-7825(91)90046-9.

[37] G. Allaire, F. Jouve, A.M. Toader, Structural optimization using sensitivity analysis and a level-set method, J. Comput. Phys. 194 (1) (2004) 363–393, https://doi.org/10.1016/j.jcp.2003.09.032.

[38] K. Kambayashi, N. Kogiso, I. Watanabe, T. Yamada, Level-set-based topology optimization of a morphing flap as a compliant mechanism considering finite deformation analysis, Struct. Multidiscip. Optim. 66 (10) (2023) 223, https://doi.org/10.1007/s00158-023-03670-1.

[39] G. Allaire, L. Cavallina, N. Miyake, T. Oka, T. Yachimura, The homogenization method for topology optimization of structures: old and new, Interdiscip. Inf. Sci. 25 (2) (2019) 75–146, https://doi.org/10.4036/iis.2019.B.01.

[40] W. Zhang, G. Dai, F. Wang, S. Sun, H. Bassir, Using strain energy-based prediction of effective elastic properties in topology optimization of material microstructures, Acta Mech. Sin. 23 (1) (2007) 77–89, https://doi.org/10.1007/s10409-006-0045-2.

[41] J. Gao, Z. Luo, L. Xia, L. Gao, Concurrent topology optimization of multiscale composite structures in Matlab, Struct. Multidiscip. Optim. 60 (2019) 2621–2651, https://doi.org/10.1007/s00158-019-02323-6.

[42] G. Bertolino, M. Montemurro, Two-scale topology optimisation of cellular materials under mixed boundary conditions, Int. J. Mech. Sci. 216 (2022) 106961, https://doi.org/10.1016/j.ijmecsci.2021.106961.

[43] K. Liang, D. Zhu, F. Li, Macro–microscale topological design for compliant mechanisms with special mechanical properties, Comput. Methods Appl. Mech. Eng. 408 (2023) 115970, https://doi.org/10.1016/j.cma.2023.115970.

[44] T. Yamada, Y. Noguchi, Topology optimization with a closed cavity exclusion constraint for additive manufacturing based on the fictitious physical model approach, Addit. Manuf. 52 (2022) 102630, https://doi.org/10.1016/j.addma.2022.102630.

[45] S. Mukherjee, D. Lu, B. Raghavan, P. Breitkopf, S. Dutta, M. Xiao, W. Zhang, Accelerating large-scale topology optimization: state-of-the-art and challenges, Arch. Comput. Methods Eng. (2021) 1–23, https://doi.org/10.1007/s11831-021-09544-3.

[46] M. Kishida, T. Kurahashi, Proposal of a modified optimality criteria method for topology optimization analysis in 3-dimensional dynamic oscillation problems, Int. J. Numer. Methods Eng. 123 (3) (2022) 866–896, https://doi.org/10.1002/nme.6880.

[47] T. Oka, T. Yamada, Topology optimization method with nonlinear diffusion, Comput. Methods Appl. Mech. Eng. 408 (2023) 115940, https://doi.org/10.1016/j.cma.2023.115940.

[48] O. Sigmund, Design of Material Structures Using Topology Optimization, Doctoral Dissertation, Technical University of Denmark, 1994.

[49] E. Andreassen, B.S. Lazarov, O. Sigmund, Design of manufacturable 3d extremal elastic microstructure, Mech. Mater. 69 (1) (2014) 1–10, https://doi.org/10.1016/j.mechmat.2013.09.018.

[50] G. Zhang, K. Khandelwal, Computational design of finite strain auxetic metamaterials via topology optimization and nonlinear homogenization, Comput. Methods Appl. Mech. Eng. 356 (2019) 490–527, https://doi.org/10.1016/j.cma.2019.07.027.

[51] X. Li, L. Gao, W. Zhou, Y. Wang, Y. Lu, Novel 2d metamaterials with negative Poisson's ratio and negative thermal expansion, Extrem. Mech. Lett. 30 (2019) 100498, https://doi.org/10.1016/j.eml.2019.100498.

[52] U. Larsen, O. Signund, S. Bouwsta, Design and fabrication of compliant micromechanisms and structures with negative Poisson's ratio, J. Microelectromech. Syst. 6 (2) (1997) 99–106, https://doi.org/10.1109/84.585787.

[53] D. Akamatsu, Y. Noguchi, K. Matsushima, Y. Sato, J. Yanagimoto, T. Yamada, Two-phase topology optimization for metamaterials with negative Poisson's ratio, Compos. Struct. 311 (2023) 116800, https://doi.org/10.1016/j.compstruct.2023.116800.

[54] O. Grodzevich, O. Romanko, Normalization and other topics in multi-objective optimization, in: Proceedings of the Fields-MITACS Industrial Problems Workshop, 2006.

[55] C. Smith, J. Grima, K. Evans, A novel mechanism for generating auxetic behaviour in reticulated foams: missing rib foam model, Acta Mater. 48 (17) (2000) 4349–4356, https://doi.org/10.1016/S1359-6454(00)00269-X.